Physica B 692 (2024) 416387

Contents lists available at ScienceDirect

Physica B: Condensed Matter

journal homepage: www.elsevier.com/locate/physb

Computational study of the structural, mechanical, electronic, optical and thermal properties of BaLiX (X =P, As, Sb) perovskites

Md Zillur Rahman [a], Sayed Sahriar Hasan [b], Mist Shamima Akter [c], Nurhakimah Mohd Mukhtar [a], Nazifa Absar [d], Md Akib Hasan [a], Tom Ichibha [b], Ryo Maezono [b], Kenta Hongo [e], Md Ariful Islam [f,*]

[a] Faculty of Electrical Engineering & Technology, Universiti Malaysia Perlis, Perlis, 02600, Malaysia
[b] School of Information Science, JAIST, Nomi, Ishikawa, 923-1292, Japan
[c] Department of Electrical and Electronic Engineering, International Islamic University Chittagong, Kumira, Chittagong, 4318, Bangladesh
[d] Chittagong College, Chittagong, 4203, Bangladesh
[e] Research Center for Advanced Computing Infrastructure, JAIST, Nomi, Ishikawa, 923-1292, Japan
[f] Institute of Mining and Specialized Civil Engineering, TU Bergakademie Freiberg, 09599, Freiberg, Germany

ARTICLE INFO

Keywords:
DFT calculations
First-principles computation
Hexagonal structure
Perovskites
Optoelectronic
Optical properties

ABSTRACT

This study explores the structural, optical, mechanical, electronic, and thermal characteristics of ionic semiconductor compounds BaLiX (X = P, As, Sb) using Density Functional Theory (DFT). A comprehensive analysis of BaLiX (X = P, As, Sb) is conducted, proving that the estimated and observed lattice parameters coincide well and confirming mechanical stability through elastic stiffness constants. Electronic band structures reveal direct bandgap semiconductor properties with values of 0.70 eV, 0.30 eV, and 0.95 eV for BaLiP, BaLiAs, and BaLiSb, respectively, suggesting specific applications such as mid-infrared photodetectors, terahertz devices, and near-infrared sensors. Optical property analyses, including energy loss function, reflectivity, refractive index, and absorption coefficient, highlight the potential of these materials for optoelectronic and photovoltaic applications. Despite elastic anisotropy, optical anisotropy remains minimal. The materials exhibit potential for use as thermal barrier coatings (TBC) due to their comparatively lower Debye temperature (D), minimum thermal conductivity (K_{min}) and lattice thermal conductivity (kph). Moreover, heat capacity calculations and thermal coefficient of expansion are also calculated.

1. Introduction

Recent advances in the study of compounds ABC, where A = Li, Cu; B = Be, Zn, Cd, Mg; and C = As, N, P, Sb, have sparked significant interest due to their intriguing physical properties. Initial investigations by Nowotny et al. [1] and Juza et al. [2] marked the first synthesis of these materials. Since then, extensive theoretical and experimental research has delved into their structural, electrical, and optical characteristics. Many researchers have explored the electronic and optical properties of various Nowotny-Juza compounds [3–5], driven by the pressing global challenges of fuel shortages and environmental degradation caused by our reliance on fossil fuels. In this context, scientists have turned their attention to eco-friendly materials and technologies. Among these, Heusler and half-Heusler (HH) compounds have garnered notable interest in condensed matter physics. These materials are celebrated for their low toxicity, mechanical strength, high thermal stability, and spintronic potential. The discovery of Cu_2MnAl by Heusler in 1903, the first of its kind, unveiled unexpected ferromagnetic properties. Half-Heusler compounds, with their general formula ABC, are derived from breaking the symmetry of Heusler compounds and feature non-centrosymmetric structures. These materials are versatile, finding applications in thermoelectric and photovoltaic systems. Their appeal is further enhanced by intriguing properties such as half-metallicity, magnetism, and thermoelectric behavior, coupled with a straightforward crystal structure.

Theoretical investigations have played a crucial role in understanding these compounds. For example, Rehman and colleagues [4] used ab initio methods to explore the structural, magnetic, electrical, and elastic properties of ScTiX materials (where X = In, Ti, Si, Sb, Ge, Pb). Similarly, Chamni et al. [5] applied first-principles methods to study the structural,

* Corresponding author.
E-mail address: Md-Ariful.Islam@mabb.tu-freiberg.de (M.A. Islam).

https://doi.org/10.1016/j.physb.2024.416387
Received 3 June 2024; Received in revised form 3 August 2024; Accepted 5 August 2024
Available online 5 August 2024

Table 1
Optimized lattice parameters (a, b, c) and unit cell volume (v) of BaLiX (X = P, As, Sb) materials.

Compound	a (Å)	b(Å)	c(Å)	v(Å^3)	Ref.
BaLiP	4.42	4.42	4.52	88.30	This work
BaLiAs	4.53	4.53	4.61	94.60	This work
BaLiSb	4.94	4.94	9.18	224.02	This work
LiBeP	3.61	3.61	5.99	78.06	[15]
LiBeAs	3.74	3.74	6.17	86.30	[15]

electronic, and elastic properties of FeVZ compounds (where Z = P and As). Miri et al. [6] examined how pressure affects the structural and optoelectronic properties of LiZP compounds (where Z = Mg, Zn, Ca). Rajendran A. and John R [7]. also investigated the electronic, structural, elastic, and anisotropic properties of HfRhA compounds (where A = As and Sb). Additionally, Guechi et al. [7] conducted a theoretical analysis of the electronic and optical properties of LiBeZ compounds (where Z = As, Bi, and Sb) using the half-Heusler framework. Experimental studies have further enriched our understanding of these materials. Photoluminescence and scanning spectrophotometry have been used to assess the optical properties of LiMgP and LiMgAs [8], while Raman scattering has provided insights into the bonding characteristics of the tetrahedral semiconductor LiMgP [9,10]. Computational analyses have also made significant strides, uncovering zone-centered phonon resonances in LiMgP and LiMgAs [11] and calculating the vibrational features of LiMgAs during the α-phase using density functional theory with the ABINIT technique [12]. Despite these advancements, the properties of BaLiX (X = P, As, Sb) remain largely unexplored, both conceptually and experimentally. This study aims to address this gap by focusing on the structural, electrical, elastic, optical, electronic, and thermal behaviors of BaLiX compounds. Understanding these characteristics is crucial for optimizing the use of half-Heusler materials in renewable energy systems. This research endeavors to provide a detailed investigation of these materials, revealing new insights and verifying previously studied aspects.

2. Computational methods

We performed density functional theory (DFT) calculations using the Vienna Ab initio Simulation Package (VASP) [13] to evaluate the band structures, density of states (DOS), and dielectric matrix of BaLiP, BaLiAs, and BaLiSb. The Perdew-Burke-Ernzerhof (PBE) function was employed for calculatons. Atomic core orbitals were replaced using the Projector Augmented-Wave (PAW) method [14]. The core sizes of the PAW potentials were Li: [He], P: [Ne], As: [Ar]3 d^{10}, Ba: [Kr]4 d^{10}, and Sb: [Kr]4 d^{10}. The energy cutoff was set at 300 eV, higher than the most considerable recommended maximum cutoff value among the potentials we used. K-point sampling was performed using the gamma-centered scheme, with the spacing between k-points being smaller than 0.25 Å^{-1}, which is sufficient for non-metallic systems. Denser k-meshes were used for DOS calculations to achieve smooth graphs. Self-consistent field iterations were continued until the total energy and orbital energies converged within 1.0 × 10^{-6} eV. Lattice vectors and atomic positions relaxed until the interatomic forces were reduced below 2.0 × 10^{-2} eV/Å. Various optical energy-dependent parameters, such as absorption coefficient, reflectivity, loss function, and refractive index, are calculated for photon energies up to 50 eV with electric field polarization vectors along the [100] direction to analyze optical properties. The stress-strain method and VASP were performed to determine the compounds' elastic stiffness constant and mechanical properties. The 3D anisotropy models Young modulus, shear modulus, and Poisson's ratio were derived using the ELATE (Elastic Tensor Analysis) program.

3. Results and discussions

3.1. Structural properties

Li-based half-Heusler compounds are classified as semiconducting alloys, possessing a P6 $\overline{m}$ 2 space group. BaLiP exhibits Li–P bond lengths of 2.55 Å and Ba–P bond lengths of 3.41 Å. In this compound, P^{3-} ions form a distorted trigonal planar coordination with Li^{1+} and Ba^{2+} ions, similar to the structures observed in BaLiAs and BaLiSb. The lattice parameters for BaLiP are a = b = 4.42 Å and c = 4.52 Å. In BaLiAs, each As^{3-} ion is coordinated in a trigonal planar arrangement with three Li^{+} ions at bond lengths of 2.62 Å. The Ba–As bond lengths are 3.49 Å, where Ba^{2+} ions form deformed pentagonal pyramids with six As^{3-} atoms. In this structure, three Li^{1+} and six Ba^{2+} atoms are bound to As^{3-} ions in a deformed trigonal planar conTableuration. The lattice parameters for BaLiAs are a = b = 4.53 Å and c = 4.61 Å. Similarly, in BaLiSb, Li^{1+} ions exhibit a trigonal planar coordination with Sb^{3-} atoms, each bond length measuring 2.85 Å. The structure also features six Sb^{3-} atoms bonded with six Ba^{2+} ions to produce octahedra with varying sharing modes, resulting in an average Ba–Sb bond length of 3.66 Å. The coordination environment of Sb^{3-} ions in BaLiSb mirrors that of As^{3-} ions in BaLiAs. The lattice parameters for BaLiSb are a = b = 4.94 Å and c = 9.18 Å, as detailed in Table 1. Fig. 1 illustrates the hexagonal crystal structures of BaLiP, BaLiAs, and BaLiSb.

3.2. Elastic constant

Comprehending elastic constants is essential for understanding the fundamental characteristics of crystalline solids, such as debye temperature, melting point, thermal expansion and specific heat. These constants provide vital details about a substance's mechanical properties, including elasticity, anisotropy, hardness, ductility, brittleness, bonding properties, and stability. In hexagonal formations, there are six elastic constants (C_{11}, C_{12}, C_{13}, C_{33}, C_{44}, and C_{66}), five of which are independent [16]. The value of C_{66} can be derived from C_{11} and C_{12}. These elastic constants, commonly assessed using criteria similar to the Born criteria for hexagonal lattices (as illustrated in Equation (1)), are crucial for determining a material's durability under various conditions, including pressure [17].

$$\begin{aligned} &C_{11} > 0, C_{33} > 0, C_{44} > 0 \\ &(C_{11} - C_{12}) > 0 (2) \\ &(C_{11} + C_{12})C_{33} - 2C_{13}^2 > 0 \end{aligned} \quad 1$$

Our determined elastic constants, detailed in Table 2 and displayed in Fig. 2, satisfy the required standards, proving the mechanical stability of BaLiX (X = P, As, Sb)'s hexagonal phase. These outcomes concur with those published before [18–24]. Furthermore, under pressure, the elastic constants meet the Born stability criterion. C_{12} and C_{44} show a rise with pressure, suggesting improved resistance to shear deformation. Additionally, C_{33} outperforms C_{11} under pressure, indicating a notable improvement in chemical bonding. We obtained the shear modulus (G), young modulus (Y) and bulk modulus (B) for BaLiX (X = P, As, Sb) from the specific elastic constants, C_{ij}, utilizing the Voigt and Reuss approximations [20]. The shear modulus (G_V) and bulk modulus (B_V) of a hexagonal lattice, under the Voigt approximation, are determined by as following equations [21,22].

$$B_v = \frac{1}{2}[2(C_{11} + C_{12}) + 4C_{13} + C_{33}] \quad 2$$

$$G_v = \frac{1}{30}(C_{11} + C_{12} + 2C_{33} - 4C_{13} + 12C_{44} + 12C_{66}) \quad 3$$

The shear modulus (G_R) besides the bulk modulus (B_R) within the Reuss approximation is expressed as [17]:

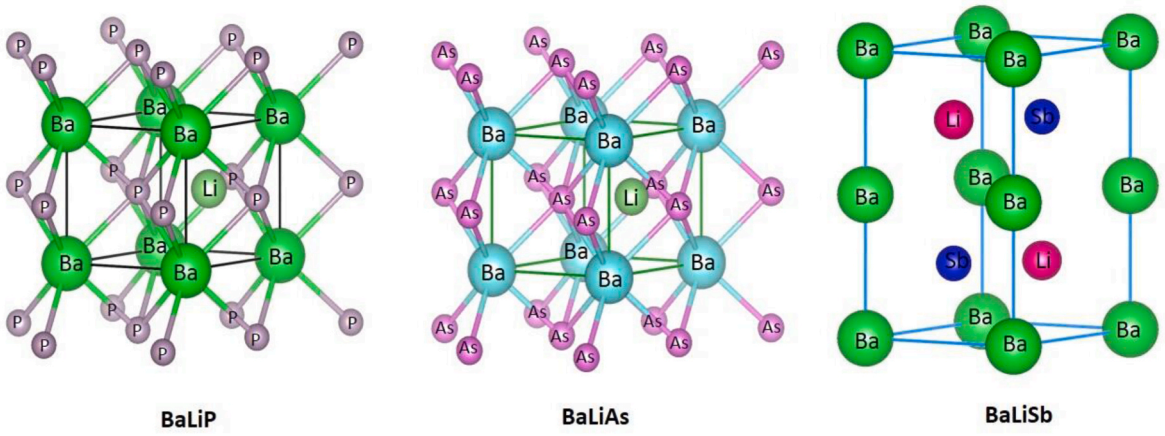

Fig. 1. Crystal structures of BaLiX (X = P, As, Sb).

Table 2
The calculated elastic constants C_{ij}(in GPa) of BaLiX (X = P, As, Sb) compounds.

Compound	C_{11}	C_{22}	C_{33}	C_{44}	C_{55}	C_{66}	C_{12}	C_{13}	C_{23}	Ref.
BaLiP	79	79	85	18	18	28	23	13	13	This work
BaLiAs	72	72	75	17	17	26	20	12	12	This work
BaLiSb	66	66	44	25	25	27	12	18	18	This work
LiBeAs	208.7	151	97	83.2	37	13	8.3	21	21	[7]
LiBeSb	145.8	127	120	54.1	44	49	13.6	18	18	[7]
LiMgP	117	65	65	48	46	46	29	51	51	[11]
LiMgAs	46.3	93	93	64.5	38	38	47.9	23	23	[11]
LiMgN	263.2	194	193	70.6	64	69	18.4	23	79	[22]
LiZnN	268.7	267	267	68.9	67	67	36.8	36	36	[22]

$$B_R = \frac{(C_{11}+C_{12})C_{33}-2C_{13}^2}{C_{11}+C_{12}+2C_{33}-4C_{13}} \quad 4$$

$$G_R = \frac{5C_{44}C_{66}\left[(C_{11}+C_{12})C_{33}-2C_{13}^2\right]}{2\left[3B_vC_{44}C_{66}+\left\{(C_{11}+C_{12})C_{33}-2C_{13}^2\right\}(C_{44}+C_{66})\right]} \quad 5$$

As Hill [24] estimated, the actual effective moduli can be calculated by taking the arithmetic mean of these two numbers. Thus, the following definitions apply to B and G:

$$B = \frac{1}{2}(B_R + B_V) \quad 6$$

$$G = \frac{1}{2}(G_R + G_V) \quad 7$$

Using the values of shear modulus (G) as well as bulk modulus (B), the relationships is used to calculate Poisson's ratio (v) besides Young's modulus (Y) [25].

$$Y = \frac{9BG}{3B+G} \quad 8$$

$$v = \frac{3B-2G}{2(3B+G)} \quad 9$$

Together with reported results [26–30], Table 3 and Fig. 2 compare the elastic moduli (Y, v, B, G, G/B). These numbers show B > G, indicating that G regulates the mechanical stability of BaLiX (X = P, As, Sb). Growing bulk modulus values suggest that chemical bonds are getting stronger. Y, inversely correlated with thermal shock resistance, suggests that BaLiX (X = P, As, Sb) has less thermal shock resistance. When a crystal's Cauchy pressure is positive, it shows ductility and damage tolerance; when it is negative, it indicates brittleness. For hexagonal materials, Cauchy pressure is defined as (C_{12} - C_{66}) and (C_{13} - C_{44}). These values are negative for BaLiX (X = P, As, Sb) compounds, implying they brittlely. Further evidence for this claim comes from the B/G ratio, which indicates whether a material is brittle or ductile. A lower B/G ratio indicates brittleness, whereas ductility is identified by a ratio greater than 1.75. Table 3 shows that the B/G ratios for BaLiX (X = P, As, Sb) compounds are less than 1.75, indicating brittleness. Similarly, the G/B ratio—referred to as Pugh's modulus—is employed to ascertain the bonding properties of atoms within a crystal. Pugh's modulus values around 0.65, 0.67, and 0.78, respectively, suggest the dominance of covalent and ionic bonding [25]. All values, as displayed in Table 3, are roughly 0.6, indicating that ionic bonding is expected in the structure. These G/B values strongly imply that ions play a significant role in interatomic bonding. The values, showing a change from covalent to ionic bonding, are also closer to 0.6. The values of Poisson's ratio (v) further support the bonding nature of the BaLiX (X = P, As, Sb) compounds. Studies indicate that ionic materials typically have a ν value of 0.25, whereas low Poisson's ratio (v) values around 0.1 correspond to covalent materials [28]. Table 3 and Fig. 2 displays that all of the ν values are close to 0.25, indicating that the structure's bonding nature is mainly ionic. Chen et al.'s semi-empirical approach, based on Pugh's modulus ratio [28], was used to compute the hardness (H_v) values (see Table 4).

$$H_V = 2\left(k^2G\right)^{0.585} - 3; (k = G/B) \quad 10$$

Table 3 shows that BaLiAs has the lowest hardness (4.8 GPa), while BaLiSb has the greatest (6.45 GPa). For BaLiX (X = P, As, Sb) compounds, all computed hardness values fall below the superhardness threshold. The machinability index μ_M is calculated as B/C_{44} and is used to evaluate a material's machinability alongside the bulk modulus (B) and C_{44}. A higher μ_M value indicates better machinability. In contrast to some previously investigated compounds, this study's μ_M exhibits a non-monotonic trend and reaches its maximum value of 2.10 for BaLiP, suggesting improved machinability. All findings are compared in Fig. 2.

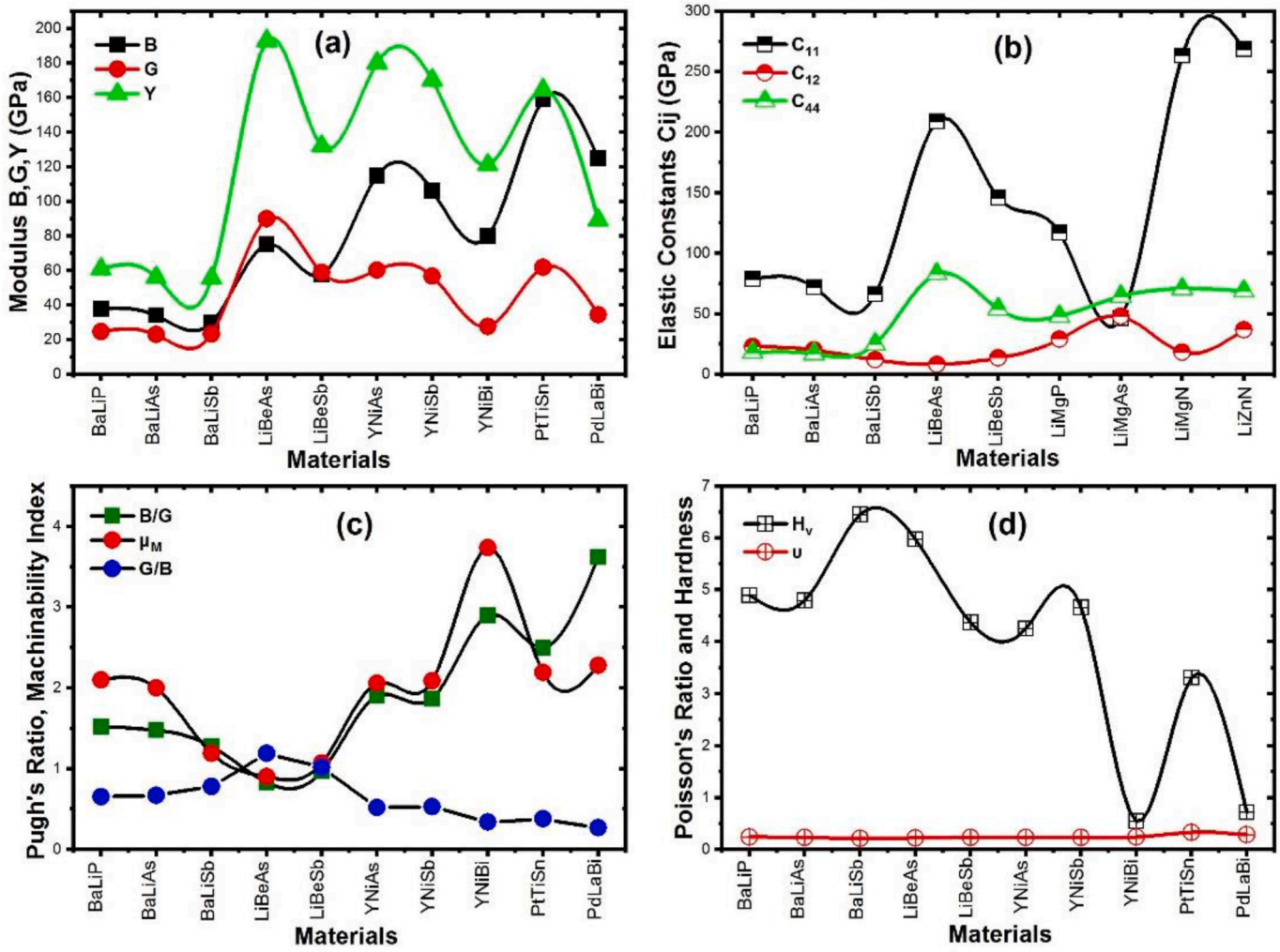

Fig. 2. (a) Bulk, shear and Young's modulus; (b) Elastic stiffness constants; (c) Pugh's ration and machinability index; (d) Poisson's ration and Hardness of BaLiX (X = P, As, Sb).

Table 3
Computed bulk modulus B (GPa), shear modulus G (GPa), Young's modulus Y (GPa), Pugh's ratio (B/G), Poisson's ratio (**υ**), machinability index, μ_M and hardness (H_v) of BaLiX (X = P, As, Sb) compounds.

Compound	B	G	Y	υ	*G/B*	B/G	μ_M	H_v	Ref.
BaLiP	37.88	24.78	61.03	0.24	0.65	1.52	2.10	4.9	This work
BaLiAs	34.09	22.9	56.17	0.23	0.67	1.48	2.0	4.8	This work
BaLiSb	29.92	23.37	55.62	0.21	0.78	1.28	1.19	6.45	This work
LiBeAs	75.1	90	192.8	0.22	1.19	0.83	0.90	5.98	[7]
LiBeSb	57.7	58.9	131.9	0.23	1.02	0.97	1.07	4.37	[7]
YNiAs	114.9	60.4	180	0.23	0.52	1.90	2.06	4.26	[34]
YNiSb	106.3	56.7	170.1	0.23	0.53	1.87	2.09	4.66	[34]
YNiBi	79.92	27.53	121.2	0.24	0.34	2.9	3.74	0.55	[34]
PtTiSn	158.8	61.9	164.5	0.33	0.38	2.5	2.19	3.31	[35]
PdLaBi	124.9	34.5	89.2	0.29	0.27	3.62	2.28	0.72	[35]

3.3. Elastic anisotropy

Elastic anisotropy plays a crucial role in various mechanical operations, including plastic distortions in crystals, quantum point positioning, small-scale splitting in ceramics, greater mobility of charged imperfections, and plastic deformation of thin films. Numerous anisotropy indices are used to describe the elastic anisotropy in crystalline materials. This study computed the shear anisotropic factors (A_1, A_2 and A_3) using the following equations [24] for BaLiX (X = P, As, Sb).

$$A_1 = \frac{(C_{11} + C_{12} + 2C_{33} - 4C_{13})}{6C_{44}} \quad (11)$$

$$A_2 = \frac{4C_{44}}{C_{11} + C_{33} - 2C_{13}} \quad (12)$$

$$A_3 = \frac{(C_{11} + C_{12} + 2C_{33} - 4C_{13})}{3(C_{11} - C_{12})} \quad (13)$$

To precisely evaluate the elastic anisotropy of crystals, Ranganathan

Table 4
Different anisotropic factors (A_1, A_2, and A_3), rate of anisotropy (A_B and A_G) and A^U (universal anisotropy index) of BaLiX (X = P, As, Sb) compounds.

Compound	A_1	A_2	A_3	A_B (GPa)	A_G (GPa)	A^U	Ref.
BaLiP	1.61	1.89	3.43	0.51	0.93	0.41	This work
BaLiAs	1.51	1.79	3.22	0.69	0.89	0.38	This work
BaLiSb	1.70	1.56	4.76	0.58	0.91	0.27	This work
LiBeAs	3.30	5.53	6.67	–	–	1.79	[7]
LiBeSb	1.12	1.19	1.83	–	–	0.04	[7]

and Ostoja-Starzewsky [26] developed the idea of the "Universal Anisotropy Index" (A^U) which is defined as:

$$A^U = 5\frac{G_V}{V_R} + \frac{B_V}{B_R} - 6 \geq 0 \quad (14)$$

The formula [27] illustrates how to compute an additional elastic anisotropy rate for hexagonal crystals using the proportion in linear compressibility indices. The following formulas [27,29] can be used to characterize anisotropies in shear moduli and compressibility:

$$A_B = \frac{B_V - B_R}{B_V + B_R} \quad (15)$$

$$A_G = \frac{G_V - G_R}{G_V + G_R} \quad (16)$$

Any divergence from unity in A_i (i = 1, 2, 3) implies elastic anisotropy in crystals. The result of the departure from unity determines the extent of elastic anisotropy along distinct planes [31,32]. Table 4 shows that BaLiX (X = P, As, Sb) is anisotropic because the value of A_i deviates from unity.

In addition, an isotropic crystal should ideally have a zero universal anisotropy index ($A^U = 0$); however, a positive number denotes some anisotropy in the crystal. Furthermore, a smaller value of A^U indicates a negligible departure from the spherical shape of the 3D contour plots of BaLiX (X = P, As, Sb). Projections of G, Y, and v (2D and 3D) give a clear picture of the anisotropy level of the material. For an anisotropic

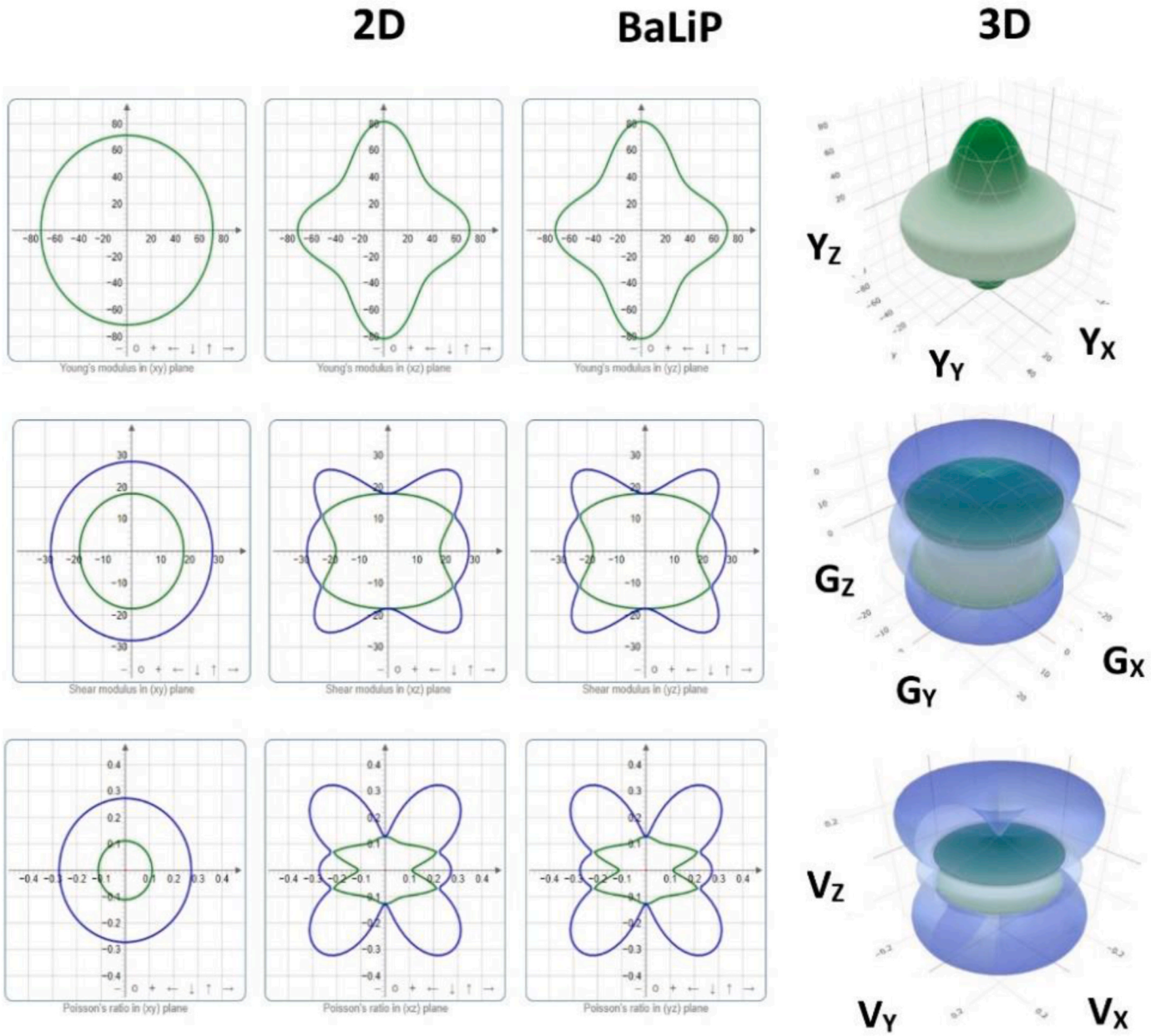

Fig. 3. Direction dependency (anisotropy) of Young's modulus (Y), shear modulus (G), and Poisson's ratio (ν) in 2D and 3D contour plots of BaLiP.

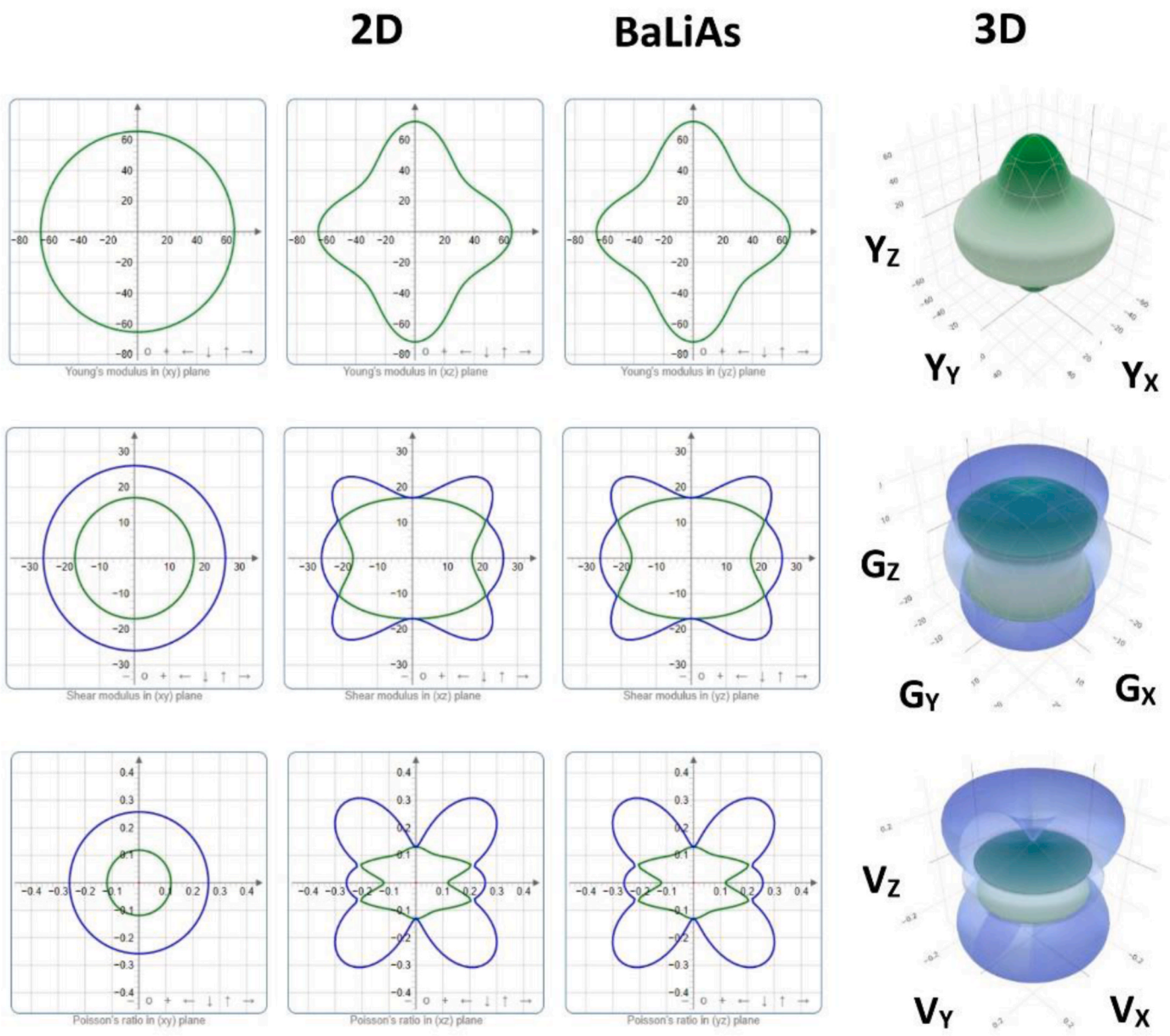

Fig. 4. Direction dependency (anisotropy) of Young's modulus (Y), shear modulus (G), and Poisson's ratio (ν) in 2D and 3D contour plots of BaLiAs.

material, these shapes will deviate from a perfect circle or sphere [30–33]. In the xy plane along the [001] direction, the plots for BaLiP (Fig. 3), BaLiAs (Fig. 4), and BaLiSb (Fig. 5) are displayed, with blue and green denoting the highest and lowest values, respectively. In isotropic materials, these polycrystalline characteristics are constant in all directions across all surfaces, producing circular forms in 2D projections and perfect spheres in 3D [34,35]. Any variation from these ideal shapes indicates anisotropy; larger deviations correspond to more substantial anisotropy. In this context, [ijk] and (ijk) represent the symmetry axis and plane, respectively. Complete isotropy is indicated by A_1, A_2, and A_3 values of 1, while deviations from 1 indicate elastic anisotropy. Positive, lower, or higher values of the anisotropic factor (A_1, A_2, and A_3) indicate in-plane focusing or defocusing, respectively.

The VASP algorithm [32] was used to calculate the directional dependency of the Poisson's ratio, shear modulus, and Young's modulus. Deviations from spherical shapes in the charts representing these physical parameters indicate the degree of anisotropy. Additionally, Table 5 provides a list of these parameters' maximum and minimum values for each component. The anisotropy indices help assess the degree of mechanical anisotropy in materials, as do the graphical explanations (2D and 3D) of elastic moduli, shown in Figs. 3–5. The anisotropic properties of materials are emphasized by the 2D and 3D projections of Young's modulus (Y), Poisson's ratio (v), and shear modulus (G). For BaLiX (X = P, As, Sb) structures, 2D and 3D representations of these features have been produced using the ELATE algorithm [34–38] and the moduli's maximum and minimum values, which were determined using the ELATE algorithm and stiffness constants.

3.4. Electronic properties

Understanding the connection between crystalline solids' physical characteristics and their crystal structure requires an investigation of the electronic band structure [30–33]. This analysis provides insights into charge transfer, electrical resistivity, and material optical properties. Furthermore, a strong understanding of band structure analysis is essential for solid-state electronics, such as solar cells and transistors. It illustrates how variations in momentum affect the energy levels of allowable electronic states within the reciprocal lattice space. Fig. 6

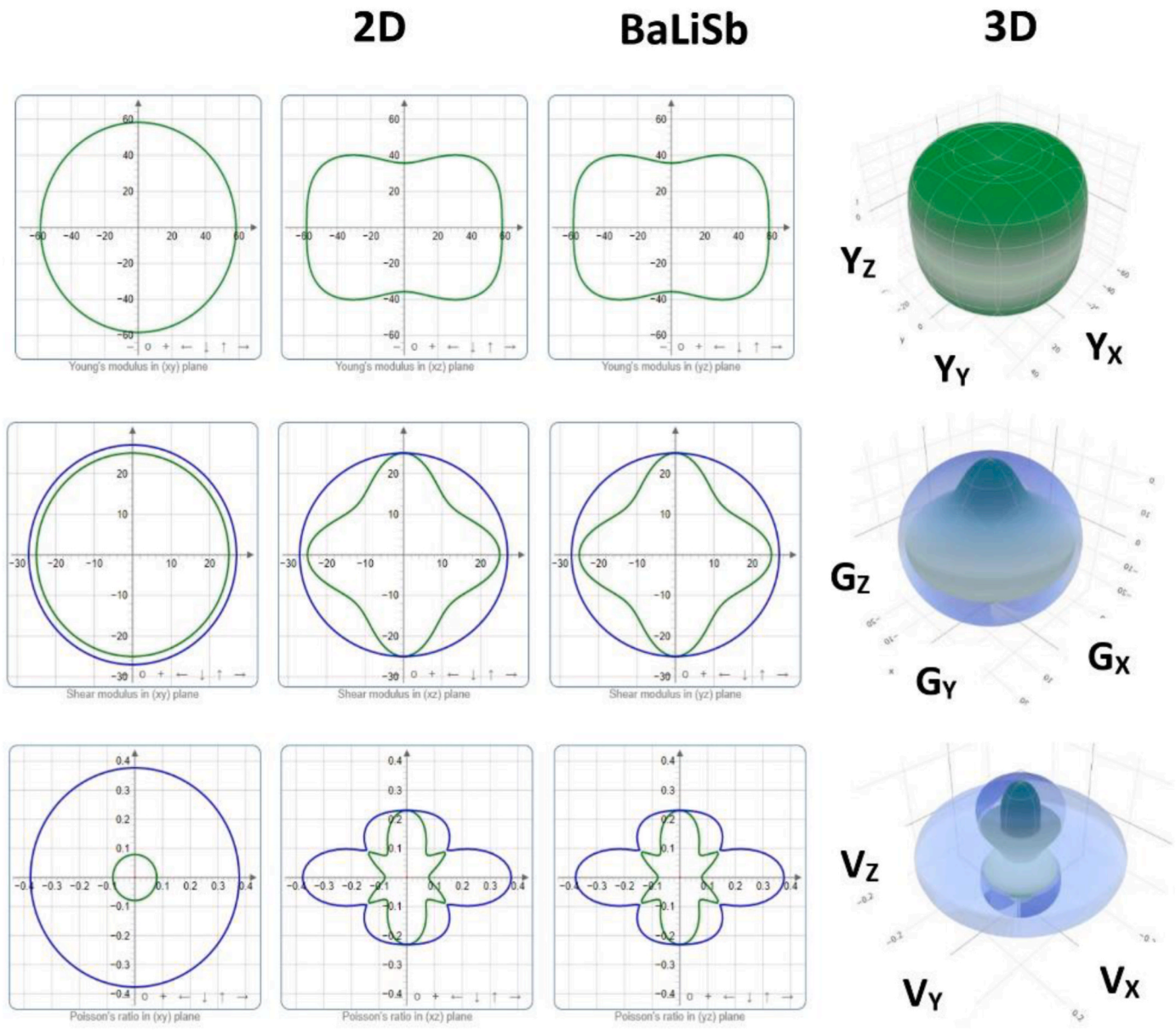

Fig. 5. Direction dependency (anisotropy) of Young's modulus (Y), shear modulus (G), and Poisson's ratio (ν) in 2D and 3D contour plots of BaLiSb.

Table 5
The lowest and highest values for Young's modulus, Poisson's ratio and Shear modulus for BaLiX (X = P, As, Sb).

Compounds	Young's modulus		Poisson's ratio		Shear modulus		Ref.
	Y_{min}(GPa)	Y_{max}(GPa)	ν_{min}(GPa)	ν_{max}(GPa)	G_{min}(GPa)	G_{max}(GPa)	
BaLiP	50.74	81.68	0.119	0.412	18	34.02	This work
BaLiAs	47.35	71.87	0.122	0.394	17	30.4	This work
BaLiSb	35.69	60.84	0.079	0.376	17.20	27	This work
LiBeAs	44.2	146.4	0.06	0.70	13	72	[7]
LiBeSb	105.8	118.7	0.11	0.21	44	52.5	[7]

displays the electronic band structure for BaLiX (X = P, As, Sb), determined along the particular lines linking the upper symmetry positions of the initial Brillouin zone. The horizontal dotted line at 0 eV represents the Fermi energy level (E_F). The Brillouin zone route (G-M-K-G-A-L-H at E_F) has a band gap situated between the conduction and valence bands, suggesting that BaLiX (X = P, As, Sb) is consistent with experimental results showing this combination to be a very effective electrical semiconductor. The direct band gaps of BaLiP, BaLiAs, and BaLiSb are 0.70 eV, 0.30 eV, and 0.95 eV, respectively, at the G point using the PBE function. The partial density of states (PDOS) provides further insight into the electrical characteristics of BaLiX (X = P, As, Sb). Figs. 7–9 represent the total density of states for BaLiP, BaLiAs, and BaLiSb, respectively, along with the partial density of states. The Density of States (DOS) analysis for BaLiP indicates it is a semiconductor, with a finite value at the Fermi level (0 eV) as seen in Fig. 7. The valence bands, spanning from −4 eV to 0 eV and primarily composed of P-p states with

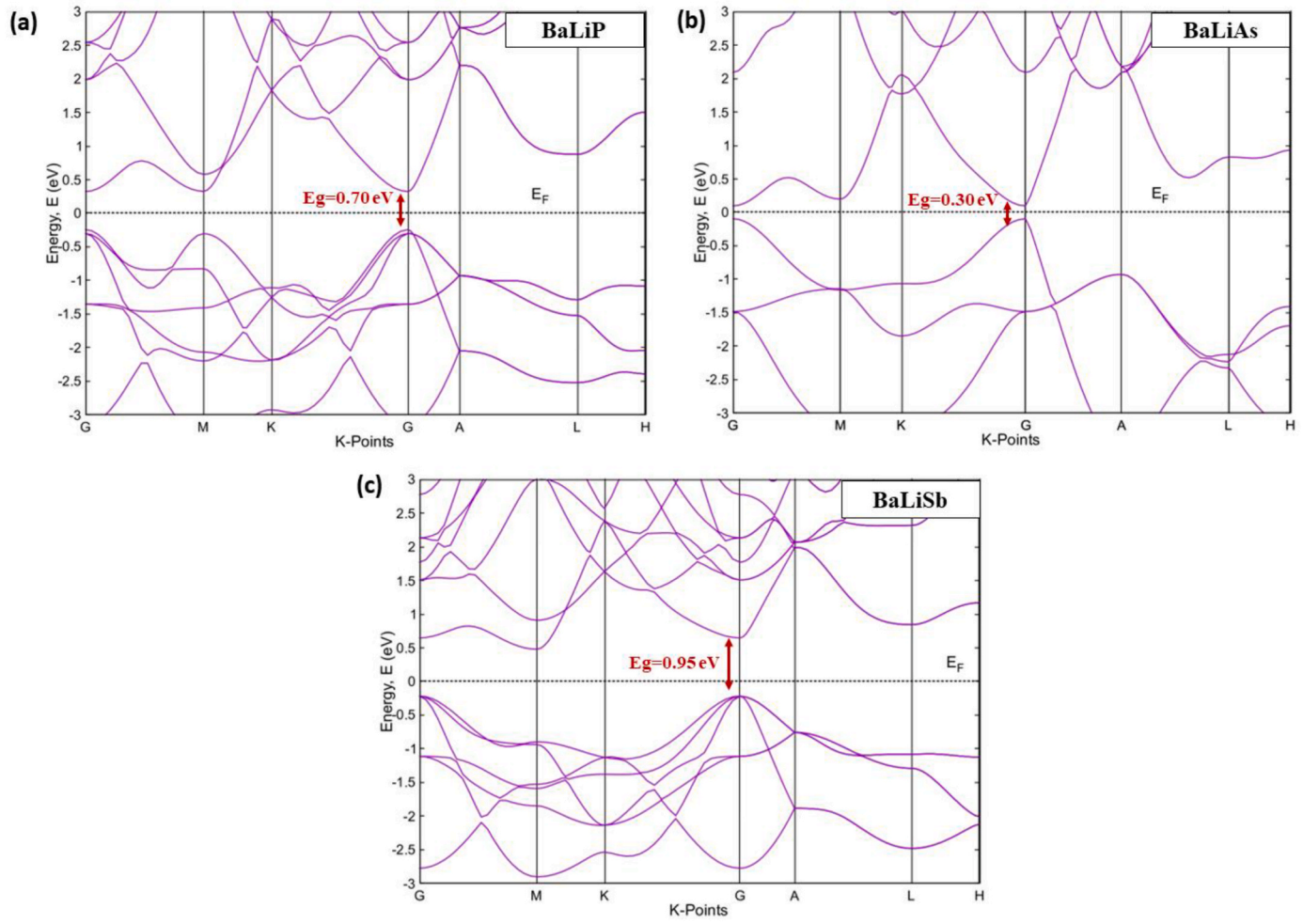

Fig. 6. Band structure of (a) BaLiP, (b) BaLiAs and (c) BaLiSb.

significant contributions from Li-p and Ba-d states, show strong covalent bonding. Ba-d states are the main constituents of the conduction bands above 0 eV and are crucial for electronic transitions. Li-s, Ba-s, and P-d antibonding states illustrate intricate electrical interactions. In Fig. 8, strong covalent bonding within BaLiAs is shown by the valence bands, primarily made up of As-p states with notable contributions from Li-p and Ba-d states. Above 0 eV, Ba-d states dominate the conduction bands, which are essential for electronic transitions.

The occurrence of antibonding states, including Li-s, Ba-s, and Sb-d states, indicates complex electronic interactions. For BaLiSb, covalent bonds are seen in the valence bands, mainly made up of Sb-p states with contributions from Li-p and Ba-d states, as shown in Fig. 9. After 0 eV, the conduction bands are primarily defined by Ba-d states, which are essential for electronic transitions. The existence of Li-s, Ba-s, and Sb-d antibonding states indicates intricate electrical interactions in the substance. The characteristics of BaLiX (X = P, As, Sb) emphasize its potential for semiconductor and optoelectronic applications. The valence band maximum (VB_{max}) and conduction band minimum (CB_{min}) of the material are found in the Brillouin Zone (BZ) center, often referred to as the G-point. Consequently, the band corner in BaLiX (X = P, As, Sb) belongs to Γ – Γ (direct type).

3.5. Optical properties

To verify the electronic structure, optical characteristics are essential. We have investigated the BaLiX (X = P,As,Sb) perovskites' absorption, reflectivity, refractivity, and loss function. We have predicted distinct optical properties of BaLiX (X = P,As,Sb) across different photon energy levels by evaluating the frequency-dependent dielectric function $\varepsilon(\omega) = \varepsilon_1(\omega) + i\varepsilon_2(\omega)$ and it is closely correlated to the electronic configuration [38–41].

$$\varepsilon_1(\omega) = 1 + \frac{2}{\pi} P \int_0^{\infty} \frac{\omega' \varepsilon 2(\omega')}{\omega' 2 - \omega^2} d\omega \quad (17)$$

The light frequency is represented by ω in the equation above, and the integral part's primary value is shown by P. Using the momentum matrix elements and accounting for all potential transitions between occupied and unoccupied electronic states, the imaginary component, $\varepsilon_2(\omega)$, is directly determined [42–44].

$$\varepsilon_2(\omega) = \frac{2e^2\pi}{\Omega\varepsilon_0} \sum_{k,v,c} \left|\psi_k^c \left|u \cdot r\right| \psi_k^v\right|^2 \delta\left(E_k^c - E_k^v - E\right) \quad (18)$$

The input electric field's polarization is represented by vector u, and ν signifies the frequency of light. ψ_k^c and ψ_k^v denote the wave functions of the conduction and valence bands at k, respectively. The reflectivity, loss function, absorption, refractive index, and conductivity, among other optical attributes, can be calculated utilizing the provided formula [38–47].

$$n(\omega) = \left[\sqrt{\varepsilon_1^2(\omega) + \varepsilon_2^2(\omega)} + \varepsilon_1(\omega)\right]^{\frac{1}{2}} \Big/ \sqrt{2} \quad (19)$$

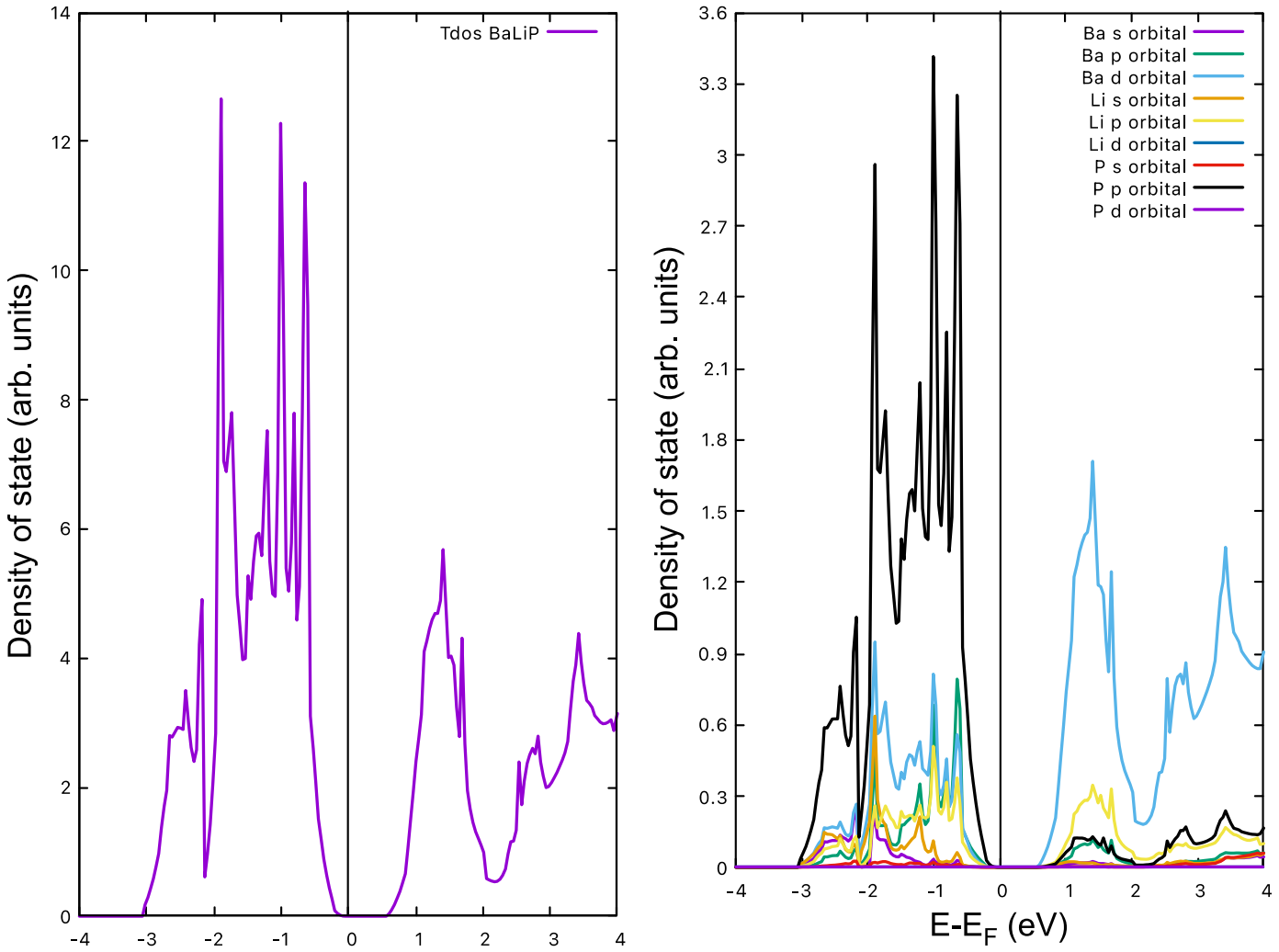

Fig. 7. Density of state for BaLiP.

$$R(\omega) = \left[\frac{(\varepsilon(\omega)^{\frac{1}{2}} - 1)}{(\varepsilon(\omega)^{\frac{1}{2}} + 1)}\right]^2 \quad (20)$$

$$L(\omega) = \frac{\varepsilon_2(\omega)}{\varepsilon_1^2(\omega) + \varepsilon_2^2(\omega)} \quad (21)$$

$$\alpha(\omega) = \sqrt{2\omega}\left(\sqrt{\varepsilon_1{}^2(\omega) + \varepsilon_2{}^2(\omega)} - \varepsilon_1(\omega)\right)^{\frac{1}{2}} \quad (22)$$

$$\sigma(\omega) = \frac{\omega\varepsilon_2}{4\pi} \quad (23)$$

Absorption shows how much light can be absorbed by the materials at particular energies (wavelengths), which sheds light on the efficiency of solar energy conversion [39,40]. This absorption spectrum is determined by the material's band gap, which governs it. The absorption is triggered by the transition of electrons from the valence band to the conduction band [39]. BaLiX (X = P,As,Sb)'s absorption spectra are displayed in Fig. 10, emphasizing the material's semiconducting character with spectra beginning at 1.5 eV, its threshold energy. The spectrum of the absorption coefficient α(ω) indicates the degree of light intensity reduction per unit length [45–47]. In Fig. 10, the optical absorbance spectra are 1.7 × 10^6 cm^{-1} for BaLiP, 1.9 × 10^6 cm^{-1} for BaLiAs, and 1.3 × 10^6 cm^{-1} for BaLiSb. BaLiP shows high absorption peaks around 7 eV and 13 eV, while BaLiAs and BaLiSb have significant absorption peaks around 13 eV and 5 eV, respectively. Reflectivity quantifies the proportion of light that a substance reflects upon exposure. It is determined by dividing the energy of the incident wave by the energy reflected from the surface. The reflectivity spectra of the three BaLiX (X = P,As,Sb) materials are shown in Fig. 10.

The reflectivity characteristics of the three compounds are almost the same. BaLiX (X = P,As,Sb) has a reflectivity of 0.45, 0.48 and 0.52 at the 6–8 eV energy range. Reflectivity for all three materials is higher at lower energies, with BaLiP peaking at 7 eV and 14 eV, BaLiAs at 5 eV and 14 eV, and BaLiSb around 6 eV and 15 eV. BaLiX (X = P,As,Sb) is hence appropriate for premium UV coating material usage. Refractivity in optical properties measures how effectively a material bends light, determined by its refractive index and related properties. Regarding refractivity, all materials show high values at lower energies, with notable peaks around 2 eV and secondary peaks at higher energies. BaLiP, BaLiAs and BaLiSb values are 3.9, 3.8 and 4.4 respectively. A material's energy loss function, which also describes plasma oscillations, quantifies the energy lost by a rapid electron moving through a molecule. The absorption and reflection characteristics of the material are connected to this function. The loss functions for BaLiX (X = P,As,Sb) are shown in Fig. 10. The peak values for loss function of BaLiP, BaLiAs and BaLiSb are 0.8, 1.1 and 1.6, respectively. These optical properties suggest that BaLiP can be more suitable for high-energy applications due to its higher absorption and lower loss function. At the same time, BaLiAs and BaLiSb could be optimized for applications requiring high reflectivity and refractivity at lower energies.

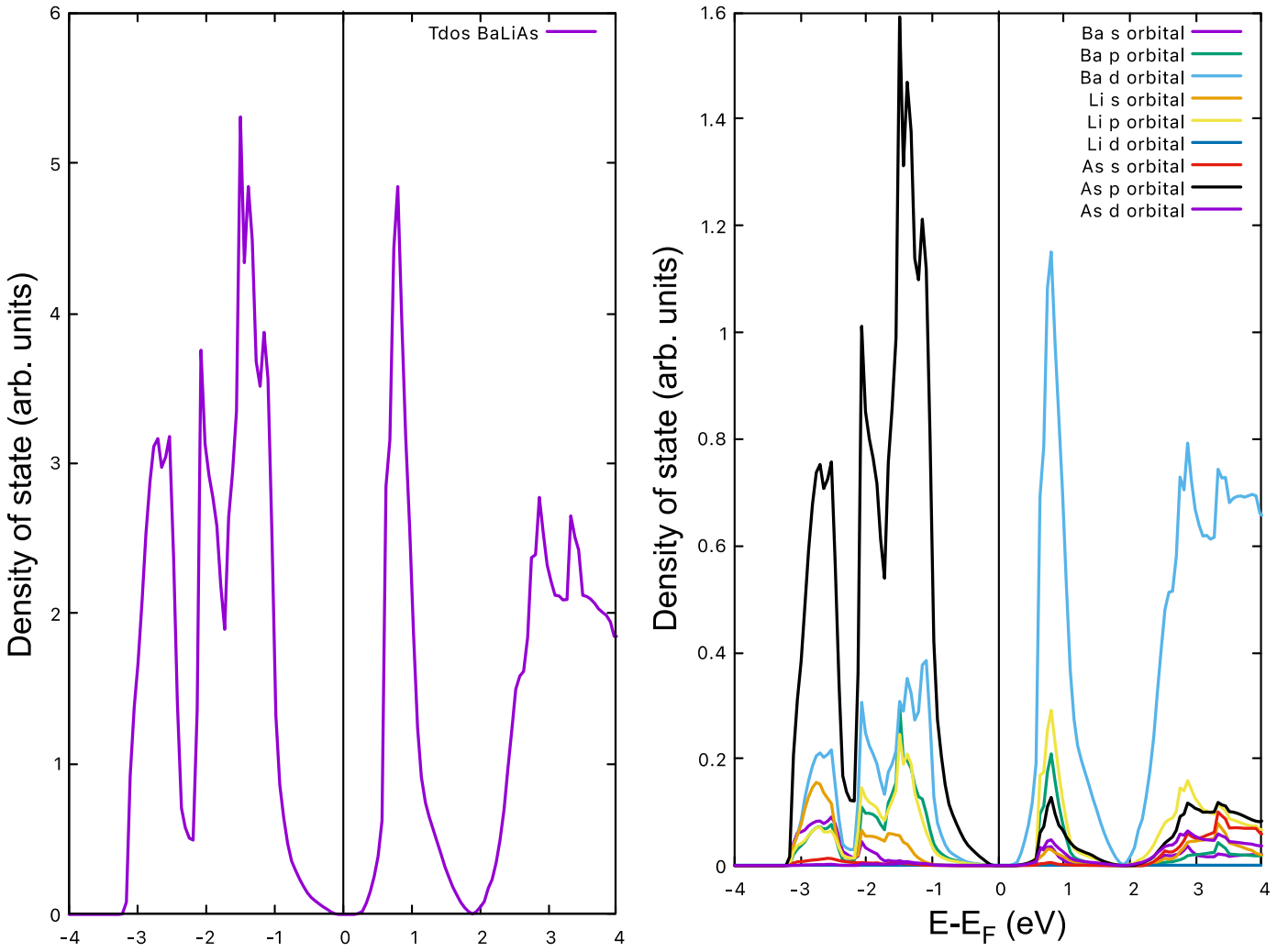

Fig. 8. Density of state for BaLiAs.

3.6. Thermal properties

In materials exploration, the Debye temperature is a crucial attribute impacting specific heat, lattice vibrations, melting point, thermal expansion, and thermal conductivity. It aids in distinguishing between high and low-temperature regions within a solid. Utilizing the assumption regarding average sound velocity and elastic constants [47–50], the Debye temperature can be calculated.

$$\theta_D = h/k_B \left[\left(3n/4\pi \right) N_A \rho \Big/ M \right]^{\frac{1}{3}} v_m \quad (24)$$

Planck's constant is denoted by h, Avogadro's number by N_A, the average sound velocity by v, and the Boltzmann constant by k_B. Equation (25), which incorporates both the transverse (v_t) and longitudinal (v_l) sound velocities in a homogeneous material, offers a method to compute the sound velocity [51].

$$v_m = \left[1/3 \left(1/v_1^3 + 2/v_t^3 \right) \right]^{-1/3} \quad (25)$$

The transverse (v_t) and longitudinal (v_l) sound velocities can be formulated about the polycrystalline shear modulus (G) and bulk modulus (B) through the model established by Reuss and Voigt [52].

$$v_1 \ [(3B + 4G)/3\rho]^{1/2} \quad (26)$$

$$v_t = \left[G/\rho \right]^{1/2} \quad (27)$$

A consistent increase in D is noticed when substituting P with As, as both elements belong to the same group on the periodic table. One of the most important characteristics of a solid is its melting point. A solid reaches its melting point when its temperature reaches a point where it becomes liquid and the solid and liquid phases are in balance. The following empirical formula was presented by Fine et al. [53–55].

$$T_m = 533 + 5.91 C_{11} \quad (28)$$

Table 6 presents the findings of our empirical formula used to calculate the melting temperature. The BaLiP compound has a greater melting temperature than BaLiAs and BaLiSb, as shown by Table 6 and Fig. 11, suggesting that it may find application as a high-temperature construction material. One important metric that shows how heat is transferred through a material is the minimum thermal conductivity, or K_{min}. Thermal conductivity falls with temperature until it reaches a minimum thermal conductivity, where it stabilises. The following formula can be used to determine the minimum thermal conductivity [54–57].

$$K_{min} = k_b v_m \left(\frac{M}{n\rho N_A} \right)^{-\frac{2}{3}} \quad (29)$$

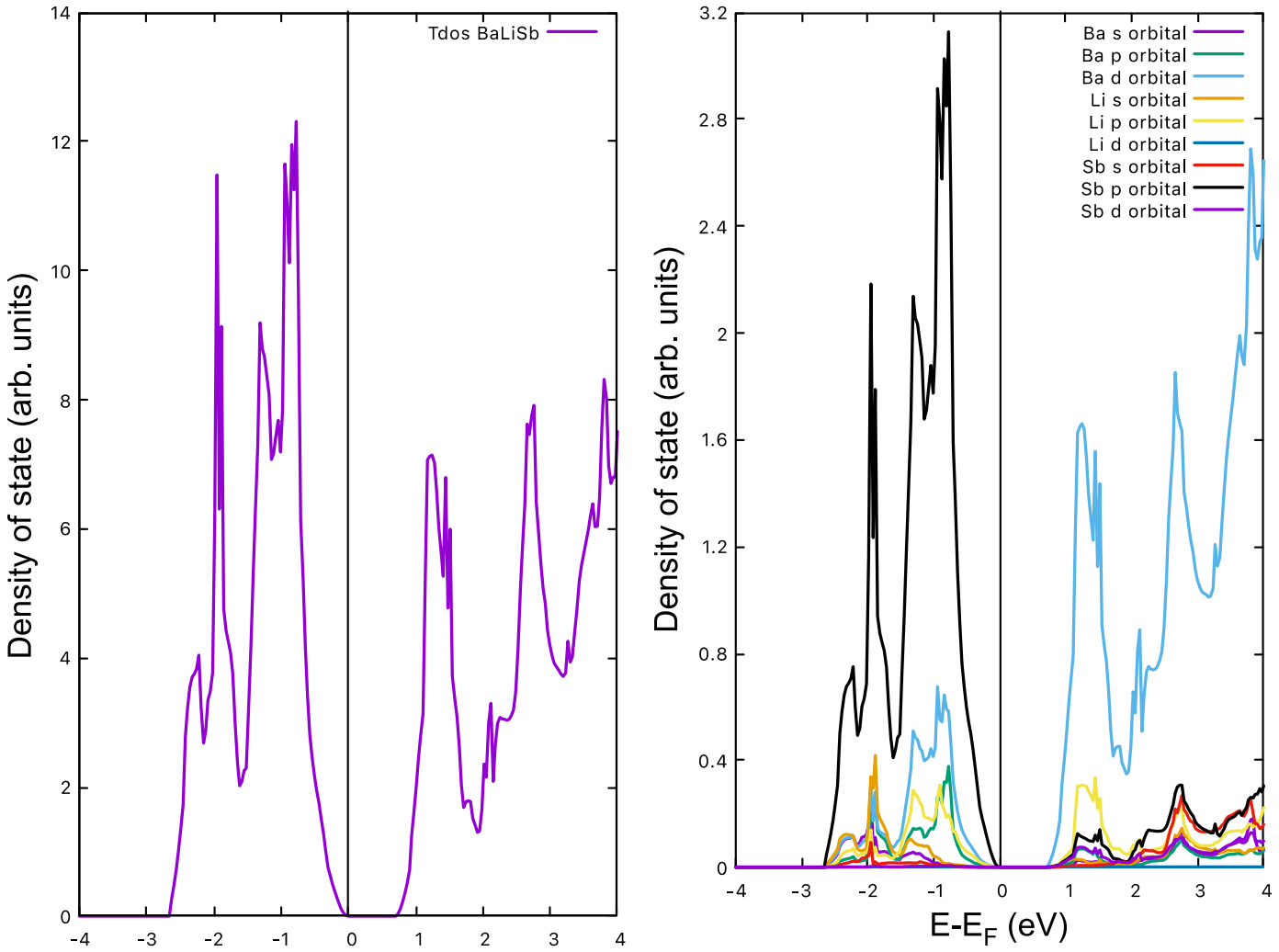

Fig. 9. Density of state for BaLiSb.

Where N is the number of atoms in a unit cell and N_A is the Avogadro number. Table 6 displays the expected lowest thermal conductivity of the perovskites under investigation. As a general rule, a low minimum thermal conductivity value is correlated with a low Debye temperature.

As Table 6 shows, a higher D typically signifies improved phonon thermal conductivity, suggesting that BaLiAs might possess superior thermal conductivity. This minimum conductivity can be determined by utilizing the minimum thermal conductivity (K_{min}) and Grüneisen parameters. As K_{min} for BaLiAs and BaLiSb are comparatively lower than that of BaLiP, it implies that BaLiAs and BaLiSb, with their lower $\boldsymbol{\theta}_D$ (287.28 K and 233.78 K) and K_{min} values (0.33 Wm−1 K^{-1} and 0.34 Wm−1 K^{-1}), could serve as an effective material for thermal barrier coatings (TBC). Fig. 11 provides a comparison of the thermodynamic properties of ABC compounds.

4. Conclusion

This research, utilizing first-principles calculations, delves into the multifaceted characteristics of BaLiX (X = P, As, Sb), covering mechanical, electrical, electronic, structural, optical, elastic, and thermal properties. The estimated and observed lattice parameters align closely, confirming mechanical stability through the elastic stiffness constants. Our findings underscore the promising potential of BaLiX (X = P, As, Sb) in the realm of semiconductor perovskites, particularly for optoelectronic applications. The direct bandgaps of BaLiX, determined using PBE, are 0.70 eV (BaLiP), 0.30 eV (BaLiAs), and 0.95 eV (BaLiSb), within the ideal range (0.30–1.0 eV) for mid-infrared photodetectors, terahertz devices, and near-infrared sensor applications. This versatility is further complemented by their impressive optical absorbance spectra, which extend across the visible range of 2–6 eV, with values of approximately 1.7×10^6 cm^{-1} (BaLiP), 1.9×10^6 cm^{-1} (BaLiAs), and 1.3×10^6 cm^{-1} (BaLiSb). Such significant absorbance highlights their capability to harness light effectively. Additionally, the reflectivity of BaLiX (X = P, As, Sb) at the 6–8 eV energy range—0.45 (BaLiP), 0.48 (BaLiAs), and 0.52 (BaLiSb)—indicates that these materials absorb a substantial amount of incoming light, further enhancing their suitability for optoelectronic device applications. The refractive indices of BaLiP, BaLiAs, and BaLiSb are 3.9, 3.8, and 4.4, respectively, showcasing their potential as high-refractive-index materials ideal for sensor construction. The loss function values for BaLiP, BaLiAs, and BaLiSb are 0.8, 1.1, and 1.6, respectively. These optical properties suggest that BaLiP, in particular, stands out for high-energy applications due to its higher absorption and lower loss function. The materials show promise for thermal barrier coatings (TBC) applications due to their relatively low Debye temperature (D), minimal thermal conductivity (K_{min}), and lattice thermal conductivity (kph).

CRediT authorship contribution statement

Md Zillur Rahman: Writing – review & editing, Writing – original draft, Visualization, Validation, Software, Resources, Methodology, Investigation, Formal analysis, Data curation, Conceptualization. **Sayed**

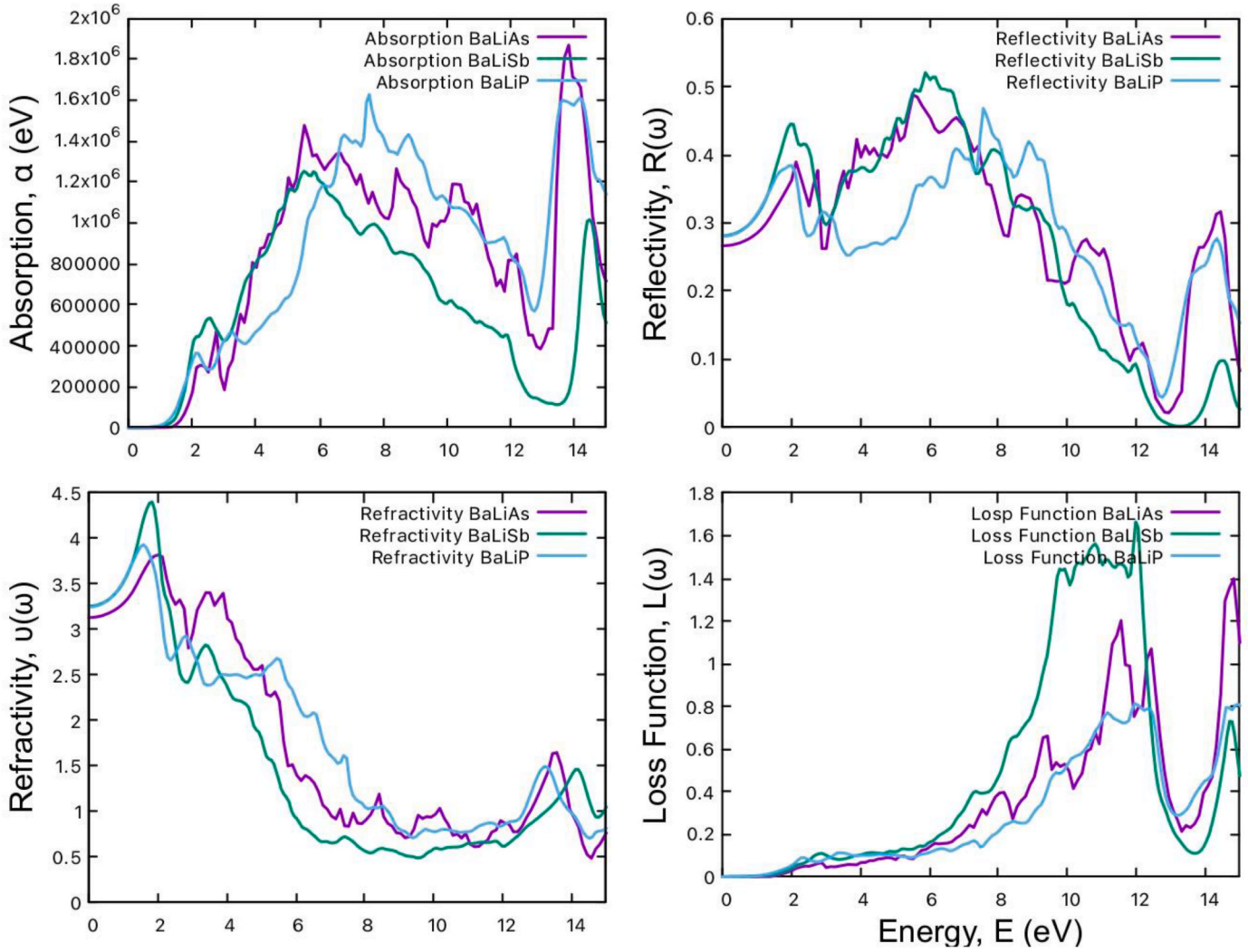

Fig. 10. Optical properties of BaLiX (X = P,As,Sb).

Table 6
The evaluated density ρ, transverse sound velocity v_t, longitudinal sound velocity v_l, average sound velocity v_m, Debye temperature θ_D, minimum thermal conductivity K_{min} and melting temperature T_m of BaLiX (X = P,As,Sb).

Compounds	ρ (g/cm^3)	v_l (K/ms)	v_t (K/ms)	v_m (K/ms)	∅ $_D$ (K)	T_m (K)	K_{min} (Wm^{-1}K^{-1})	Ref.
BaLiP	3.80	4.31	2.55	2.82	286.30	718.5	0.45	This work
BaLiAs	1.87	5.87	3.49	3.87	287.28	682.5	0.33	This work
BaLiSb	4.55	3.66	2.26	2.49	233.78	618	0.34	This work
LiBeAs	3.67	7.28	4.94	5.39	672.06	1123	1.29	[7]
LiBeSb	4.23	5.67	3.73	4.08	464.50	969	0.83	[7]
LiBeBi	6.56	4.09	2.64	2.90	323.90	762	0.50	[24]
LiScSi	3.19	8.86	2.32	2.65	251.47	915	0.64	[24]
YNiAs	6.12	3.14	5.65	3.49	383.26	1059	0.66	[34]
YNiSb	6.99	2.84	5.10	3.17	340.51	1219	0.57	[34]
YNiBi	8.64	1.78	3.67	2.00	210.53	1029	0.34	[34]

Sahriar Hasan: Software, Formal analysis, Data curation. **Mist Shamima Akter:** Visualization, Formal analysis. **Nurhakimah Mohd Mukhtar:** Supervision, Formal analysis. **Nazifa Absar:** Formal analysis. **Md Akib Hasan:** Formal analysis. **Tom Ichibha:** Supervision, Visualization, Writing – review & editing. **Ryo Maezono:** Supervision, Visualization, Writing – review & editing. **Kenta Hongo:** Supervision, Visualization, Writing – review & editing. **Md Ariful Islam:** Visualization, Supervision, Investigation, Formal analysis, Data curation, Conceptualization.

Declaration of competing interest

The authors declare the following financial interests/personal relationships which may be considered as potential competing interests: Md Ariful Islam reports was provided by TU Bergakademie Freiberg University. Md Ariful Islam reports a relationship with TU Bergakademie Freiberg University that includes: employment. If there are other authors, they declare that they have no known competing financial interests or personal relationships that could have appeared to influence the work reported in this paper.

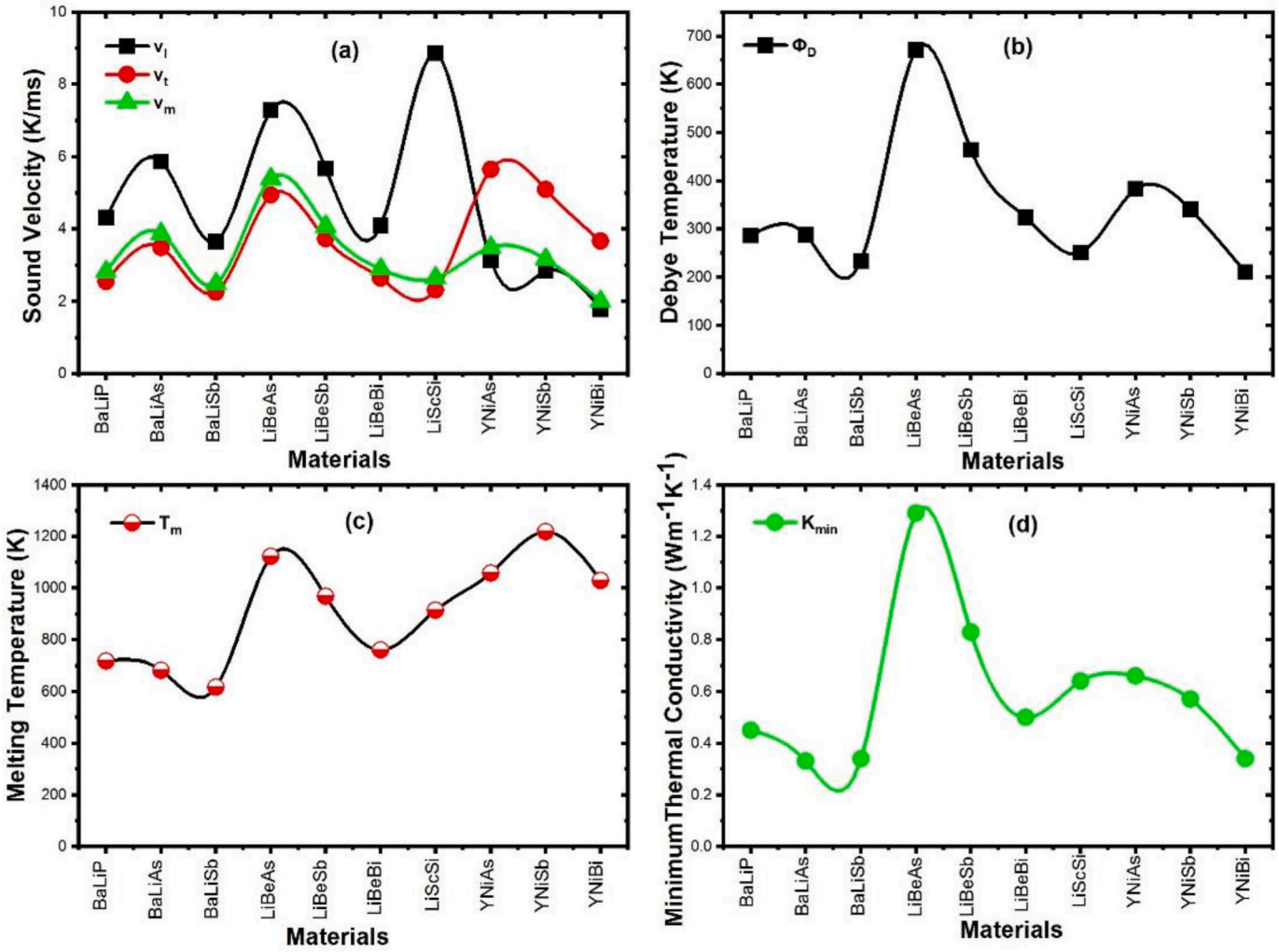

Fig. 11. (a) Sound velocity, (b) Debye Temperature (c) Melting temperature, (d) Minimum Thermal Conductivity of BaLiX (X = P,As,Sb).

Data availability

Data will be made available on request.

Acknowledgments

This study is supported by TU Bergakademie Freiberg, 09599, Germanany. The computations in this work have been partially performed using the facilities of the Research Center for Advanced Computing Infrastructure (RCACI) at JAIST. K.H. is grateful for the support from MEXT-KAKENHI, Japan (JP22H02170 and JP23H04623), and the Air Force Office of Scientific Research, United States (Award Numbers: FA2386-22-1-4065).

References

[1] L. Kalarasse, et al., Pressure effect on the optical properties of the filled tetrahedral semiconductors LiZnX (X= N, P, andAs), J. Phys. Chem. Solid. 68 (2007) 12, https://doi.org/10.1016/j.jpcs.2007.06.015.
[2] A. Mellouki, et al., First principles calculations of the structural and elastic properties of the filled tetrahedral compounds LiCdX (X= N, P, As), Comput. Mater. Sci. 42 (4) (2008) 579–583, https://doi.org/10.1016/j.commatsci.2007.09.006.
[3] A. Bouhemadou, Elastic, electronic and optical properties of the filled tetrahedral semiconductor α-LiCdAs, Mater. Sci. Semicond. Process. 12 (2009) 4–5, https://doi.org/10.1016/j.mssp.2009.11.001.
[4] N. Chami, O. Arbouche, S. Chibani, F.Z.D. Khodja, K. Amara, M. Ameri, Y. Al-Douri, M. Adjdir, J. Electron. Mater. (2020), https://doi.org/10.1007/s11664-020-08225-4.
[5] M. Miri, Y. Ziat, H. Belkhanchi, Z. Zarhri, Y. Ait-El-Kadi, Physica B: Condenser (2023), https://doi.org/10.1016/j.physb.2023.415216.
[6] Anubama Rajendran, Rita John, First principles study on electronic properties and mechanical stability of HfRhZ (Z= as and Sb) half Heusler alloys, J. Cryst. Growth 581 (2022), https://doi.org/10.1016/j.jcrysgro.2021.126468.
[7] N. Guechi, et al., Pressure induced phase transition, electronic and optical properties of LiBeX (X= As, Sb and Bi), J. Phys. Condens. Matter 32 (2020) 32, 325503.10.1088/1361-648X/ab85f2.
[8] A. Bouhemadou, et al., Theoretical prediction of the elastic, electronic and optical properties of the filled tetrahedral semiconductor α-LiMgSb, Comput. Mater. Sci. 49 (1) (2010), https://doi.org/10.1016/j.commatsci.2010.04.021.
[9] A. Bouhemadou, R. Khenata, First-principles studies of pressure dependence of elastic and electronic properties in filled tetrahedral semiconductors LiMgX (X= N, P, and As), J. Phys. Chem. Solid. 68 (2007) 4, https://doi.org/10.1016/j.jpcs.2007.01.022.
[10] F. Kalarasse, B. Bennecer, A. Mellouki, Optical properties of the filled tetrahedral semiconductors LiMgX (X= N, P and As), J. Phys. Condens. Matter 18 (2006) 31, https://doi.org/10.1088/0953-8984/18/31/018.
[11] S. Djeroud, et al., Electronic and optical properties of LiMgN, LiMgP and LiMgAs under hydrostatic pressure, J. Phys. Chem. Solid. 70 (2009) 1, https://doi.org/10.1016/j.jpcs.2008.08.015.
[12] Fethi Soyalp, et al., A first-principles study of the structural, elastic, electronic and phonon properties of LiMgP and LiMgAs in the α, β and γ phases, J. Alloys Compd. 551 (2013) 108–117, https://doi.org/10.1016/j.jallcom.2012.09.110.
[13] G. Kresse, J. Furthmüller, Phys. Rev. B Condens. Matter 54 (1996) 11169–11186, https://doi.org/10.1039/D4TC01463D.
[14] P.E. Blochl, Phys. Rev. B Condens. Matter 50 (1994) 17953–18979, https://doi.org/10.1039/D0TC04516K.
[15] Fethi Soyalp, et al., A first-principles study of the structural, elastic, electronic and phonon properties of LiMgP and LiMgAs in the α, β and γ phases, J. Alloys Compd. 551 (2013) 108–117, https://doi.org/10.1016/j.jallcom.2012.09.110.
[16] Gokhan Surucu, Investigation of structural, electronic, anisotropic elastic, and lattice dynamical properties of MAX phases borides: an Ab-initio study on

hypothetical M2AB (M= Ti, Zr, Hf; A= Al, Ga, In) compounds, Mater. Chem. Phys. 203 (2018), https://doi.org/10.1016/j.matchemphys.2017.09.050.
[17] A. Togo, F. Oba, I. Tanaka, First-principles calculations of the ferroelastic transition between rutile-type and CaCl 2 -type SiO 2 at high pressures, Phys. Rev. B 78 (2008) 134106, https://doi.org/10.1103/PhysRevB.78.134106.
[18] K. Momma, F. Izumi, P.M. J., P.C. J., H.P. J., C.S. J., P.M. C., N. T., K. Y., VESTA 3 for three-dimensional visualization of crystal, volumetric and morphology data, J. Appl. Crystallogr. 44 (2011) 1272e1276, https://doi.org/10.1107/S0021889811038970.
[19] Z. Wu, E. Zhao, H. Xiang, X. Hao, X. Liu, J. Meng, Crystal structures and elastic properties of superhard IrN2 and IrN3 from first principles, Phys. Rev. B 76 (2007) 54115, https://doi.org/10.1103/PhysRevB.76.054115.
[20] R.-K. Pan, L. Ma, N. Bian, M.-H. Wang, P.-B. Li, B.-Y. Tang, L.-M. Peng, W.-J. Ding, First-principles study on the elastic properties of B0 and Q phase in AleMgeSi (eCu) alloys, Phys. Scripta 87 (2013) 15601, https://doi.org/10.1088/0031-8949/87/01/015601.
[21] J. Chang, G.-P. Zhao, X.-L. Zhou, K. Liu, L.-Y. Lu, Structure and mechanical properties of tantalum mononitride under high pressure: a first-principles study, J. Appl. Phys. 112 (2012) 83519, https://doi.org/10.1063/1.4759279.
[22] Aron Walsh, Wei Su-Huai, Theoretical study of stability and electronic structure of Li (Mg, Zn) N alloys: a candidate for solid state lighting, Phys. Rev. B Condens. Matter 76 (19) (2007) 195208, https://doi.org/10.1103/PhysRevB.76.195208.
[23] Shivakumar I. Ranganathan, Martin Ostoja-Starzewski, Universal elastic anisotropy index, Phys. Rev. Lett. 101 (5) (2008), https://doi.org/10.1103/PhysRevLett.101.055504.
[24] A. Amudhavalli, et al., First principles study of structural and optoelectronic properties of Li based half Heusler alloys, Computational Condensed Matter 14 (2018) 55–66, https://doi.org/10.1016/j.cocom.2018.01.002.
[25] Zhimei Sun, et al., Calculated elastic properties of M2AlC (M= Ti, V, Cr, Nb and Ta), Solid State Commun. 129 (2004) 9, https://doi.org/10.1016/j.ssc.2003.12.008.
[26] Shuang Chen, Yong Pan, Noble metal interlayer-doping enhances the catalytic activity of 2H–MoS2 from first-principles investigations, Int. J. Hydrogen Energy 46 (2021) 40, https://doi.org/10.1016/j.ijhydene.2021.03.202.
[27] Shuang Chen, Yong Pan, Influence of group III and IV elements on the hydrogen evolution reaction of MoS2 disulfide, J. Phys. Chem. C 125 (2021) 22, https://doi.org/10.1021/acs.jpcc.1c03152.
[28] M.F. Yan, H.T. Chen, Structural, elastic and electronic properties of Cr2N: a first-principles study, Comput. Mater. Sci. 88 (2014) 81–85, https://doi.org/10.1016/j.commatsci.2014.02.035.
[29] M.A. Hadi, et al., Band structure, hardness, thermodynamic and optical properties of superconducting Nb 2 AsC, Nb 2 InC and Mo 2 GaC, International Journal of Computational Materials Science and Engineering 2 (2) (2013), https://doi.org/10.1142/S2047684113500073.
[30] Yong Pan, The influence of N-vacancy on the electronic and optical properties of bulk InN nitrides, Mater. Sci. Eng., B 271 (2021), https://doi.org/10.1016/j.mseb.2021.115265.
[31] Yong Pan, Jin Zhang, Influence of noble metals on the electronic and optical properties of the monoclinic ZrO2: a first-principles study, Vacuum 187 (2021), https://doi.org/10.1016/j.vacuum.2021.110112.
[32] Job W. Wafula, Structural, elastic, electronic, optical and thermal properties of YMAu (M= Si or Ge or Sn) Half-Heusler compounds; A DFT study, Results in Materials 19 (2023) 100413, https://doi.org/10.1016/j.rinma.2023.100413.
[33] Md Zillur Rahman, et al., Insight into the physical properties of the chalcogenide XZrS3 (X= Ca, Ba) perovskites: a first-principles computation, J. Electron. Mater. (2024), https://doi.org/10.1007/s11664-024-11120-x.
[34] Madhu Sarwan, Abdul Shukoor, Sadhna Singh, A first principle study of structural, elastic, electronic and thermodynamic properties of Half-Heusler compounds; YNiPn (Pn= As, sb, and bi), Solid State Sci. 112 (2021) 106507, https://doi.org/10.1016/j.solidstatesciences.2020.106507.
[35] P.O. Adebambo, et al., Assessing the structural, electronic, elastic and thermoelectric properties of PtTiSn and PdLaBi transition metal alloys from the first-principles prospective, Mater. Sci. Semicond. Process. 129 (2021) 105796, https://doi.org/10.1016/j.mssp.2021.105796.
[36] Md Zillur Rahman, Nurhakimah Mohd Mukhtar, A comprehensive study on magnetic materials selection for power electronic converters. 2023 IEEE Symposium on Computers & Informatics (ISCI), IEEE, 2023, https://doi.org/10.1109/ISCI58771.2023.10391900.
[37] Md Zahid Hasan, et al., Insights into the physical properties of newly synthesized AMn2P2 (A= Ca, Sr) via density functional theory, Phys. B Condens. Matter 653 (2023) 414651, https://doi.org/10.1016/j.physb.2023.414651.
[38] Md Atikur Rahman, et al., First-principles calculations to investigate elastic, electronic, optical and thermodynamic properties of Pt3X (X= Ti, Cu), Results Phys. 44 (2023) 106141, https://doi.org/10.1016/j.rinp.2022.106141.
[39] S.K. Mitro, et al., Insights into the physical properties and anisotropic nature of ErPdBi with an appearance of low minimum thermal conductivity, Chin. Phys. B 30 (1) (2021) 016203, https://doi.org/10.1088/1674-1056/abaf9d.
[40] O.L. Anderson, A simplified method for calculating the debye temperature from elastic constants, J. Phys. Chem. Solid. 24 (7) (Jul. 1963) 909–917, https://doi.org/10.1016/0022-3697(63)90067-2.
[41] W. Huang, H. Chen, Investigation of the elastic, hardness, and thermodynamic properties of actinide oxides, Phys. B Condens. Matter 449 (Sep) (2014) 133–137, https://doi.org/10.1016/j.physb.2014.05.024.
[42] Y. Shen, D.R. Clarke, P.A. Fuierer, Anisotropic thermal conductivity of the Aurivillus phase, bismuth titanate (Bi4Ti3O12): a natural nanostructured superlattice, Appl. Phys. Lett. 93 (10) (Sep. 2008) 102907, https://doi.org/10.1063/1.2975163.
[43] S.U. Rehman, F.K. Butt, Z. Tariq, F. Hayat, R. Gilani, F. Aleem, Pressure induced structural and optical properties of cubic phase SnSe: an investigation for the infrared/midinfrared optoelectronic devices, J. Alloys Compd. 695 (Feb) (2017) 194–201, https://doi.org/10.1016/j.jallcom.2016.10.120.
[44] P.W. Muchiri, K.K. Korir, N.W. Makau, G.O. Amolo, The impact of anionic vacancies on the mechanical properties of NbC and NbN: an ab initio study, Comput. Mater. Sci. 203 (Feb) (2022) 111113, https://doi.org/10.1016/j.commatsci.2021.111113.
[45] Md Atikur Rahman, et al., An ab-initio study to investigate the structural, mechanical, electrical, optical and thermal properties of the AZrO3 (A= Mg, Ca, Sr, Ba, Sn, Cu) compounds, Mater. Today Commun. 34 (Mar) (2023) 105339, https://doi.org/10.1016/j.mtcomm.2023.105339.
[46] J.C. Wei, H.C. Chen, W. Huang, J. Long, Theoretical investigation of the elastic, Vickers hardness and thermodynamic properties of δ -WN under pressure, Mater. Sci. Semicond. Process. 27 (Nov) (2014) 883–890, https://doi.org/10.1016/j.mssp.2014.08.041.
[47] M.U. Salma, MdA. Rahman, Physical properties of ThCr2Si2 -type Rh-based compounds A Rh2Ge2 (A = Ca, Sr, Y and Ba): DFT based first-principles investigation, Int. J. Mod. Phys. B 32 (32) (Dec. 2018) 1850357, https://doi.org/10.1142/S0217979218503575.
[48] M.K. Butt, et al., A DFT study of structural, magnetic, elastic and optoelectronic properties of lanthanide based XAlO3 (X=Nd, Gd) compounds, J. Mater. Res. Technol. 9 (6) (Nov. 2020) 16488–16496, https://doi.org/10.1016/j.jmrt.2020.11.055.
[49] M.K. Butt, et al., A DFT study of structural, magnetic, elastic and optoelectronic properties of lanthanide based XAlO3 (X=Nd, Gd) compounds, J. Mater. Res. Technol. 9 (6) (Nov. 2020) 16488–16496, https://doi.org/10.1016/j.jmrt.2020.11.055.
[50] J. Maibam, B. Indrajit Sharma, R. Bhattacharjee, R.K. Thapa, R.K. Brojen Singh, Electronic structure and elastic properties of scandium carbide and yttrium carbide: a first principles study, Phys. B Condens. Matter 406 (21) (Nov. 2011) 4041–4045, https://doi.org/10.1016/j.physb.2011.07.036.
[51] Ü. Bayhan, İ. Yilmaz, Prediction of structural, electronic, and lattice dynamical properties of ABO3 [A= K, Rb, Cs; B= Sn, Sb] perovskite compounds, Phys. B Condens. Matter 649 (2023) 414355, https://doi.org/10.1016/j.physb.2022.414355.
[52] M.A. Ali, M.M. Hossain, M.A. Hossain, M.T. Nasir, M.M. Uddin, M.Z. Hasan, A.K.M. A. Islam, S.H. Naqib, Recently synthesized (Zr1-xTix) 2AlC (0≤ x≤ 1) solid solutions: theoretical study of the effects of M mixing on physical properties, J. Alloys Compd. 743 (2018) 146–154, https://doi.org/10.1016/j.jallcom.2018.01.396.
[53] Rahman, A., Hasanb, W.H., Khatun, R., Hasan, M.Z., Rahman, M.H., Sarker, S., Hasan, M. and Lubna, J.F., Comparative study of the physical properties of lead-free perovskites Azro3 (a= Mg, Ca, Sr, Ba, Sn, Cu) through dft simulation. Zahid and Rahman, Md. Hafijur and Sarker, Sushmita and Hasan, Mahbub and Lubna, Jannatul Ferdous, Comparative Study of the Physical Properties of Lead-Free Perovskites Azro3 (a= Mg, Ca, Sr, Ba, Sn, Cu) Through Dft Simulation. https://doi.org/10.2139/ssrn.4291080.
[54] K.M. Hossain, M.H. Rubel, M.M. Rahaman, M.M. Hossain, M.I. Hossain, A. A. Khatun, J. Hossain, A.K.M.A. Islam, A comparative theoretical study on physical properties of synthesized AVO3 (A= Ba, Sr, Ca, Pb) perovskites, arXiv preprint arXiv:1905.01437 (2019), https://doi.org/10.48550/arXiv.1905.01437.
[55] Soukaina Bouhmaidi, et al., A DFT study of electronic, optical and thermoelectric properties of Ge-halide perovskites CsGeX3 (X= F, Cl and Br), Computational Condensed Matter 31 (2022) e00663, https://doi.org/10.1016/j.cocom.2022.e00663.
[56] S. Bouhmaidi, R.K. Pingak, L. Setti, First-principles investigation of electronic, elastic, optical and thermoelectric properties of strontium-based anti-perovskite Sr3MN (M= P and As) for potential applications in optoelectronic and thermoelectric devices, Moroc. J. Chem. 11 (4) (2023) 11–14, https://doi.org/10.48317/IMIST.PRSM/morjchem-v11i04.41366.
[57] Md Tarekuzzaman, et al., A systematic first-principles investigation of the structural, electronic, mechanical, optical, and thermodynamic properties of Half-Heusler ANiX (A Sc, Ti, Y, Zr, Hf; X Bi, Sn) for spintronics and optoelectronics applications, J. Comput. Chem. (2024), https://doi.org/10.1002/jcc.27455.